Bioelectrochemistry 163 (2025) 108909

Contents lists available at ScienceDirect

Bioelectrochemistry

journal homepage: www.journals.elsevier.com/bioelectrochemistry

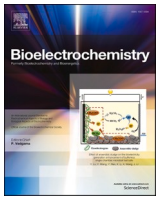

Print-Light-Synthesis of ruthenium oxide thin film electrodes for electrochemical sensing applications☆

Stefano Gianvittorio [a], Marco Malferrari [b], Horst Pick [c], Stefania Rapino [b,d], Andreas Lesch [a,*]

[a] University of Bologna, Department of Industrial Chemistry "Toso Montanari", Center of Chemical Catalysis-C^3, Via Piero Gobetti 85, 40129 Bologna, Italy
[b] University of Bologna, Department of Chemistry "Giacomo Ciamician", Via Piero Gobetti 85, 40129 Bologna, Italy
[c] Ecole Polytechnique Fédérale de Lausanne (EPFL), Environmental Engineering Institute, GR-LUD, School of Architecture, Civil and Environmental Engineering, EPFL Station 2, 1015 Lausanne, Switzerland
[d] IRCCS Azienda Ospedaliero-Universitaria di Bologna, 40138 Bologna, Italy

ARTICLE INFO

Keywords:
Inkjet printing
Photochemical reduction
Print-Light-Synthesis
Ruthenium oxide
pH sensing
Cell cultures
Amperometric sensing

ABSTRACT

Print-Light-Synthesis (PLS) combines the inkjet printing of a ruthenium precursor ink with the simultaneous photo-induced generation of ruthenium oxide films. During PLS, inkjet-printing generates on conductive as well as insulating substrates micrometer-thin reaction volumes that contain with high precision defined precursor loadings. Upon direct UV light irradiation, the Ru precursor converts to RuO_2 while all other ink components escape in the gas phase. No post PLS processes are required, and the as-obtained RuO_2 films can be immediately used as electrochemical devices. Two-dimensional RuO_2 patterns with micrometric resolution and highly-controlled ruthenium loadings (few μg/cm^2) are realized. Thin RuO_2 films are generated on insulating substrates, such as polyimide, as well as individual RuO_2 particles on conductive substrates, such as graphene layers. The RuO_2 films are characterized by electron microscopy and spectroscopic techniques. The sensoristic applicability of the PLS-RuO_2 electrodes is demonstrated by potentiometric pH sensing in cell cultures and amperometric detection of L-cysteine. For pH sensing the RuO_2 film electrodes show Nernstian sensitivity. L-cysteine detection of RuO_2-modified graphene electrodes showed an electrocatalytical effect and resulted in the possibility of selectively detecting L-Cysteine also in presence of the interfering compound uric acid.

1. Introduction

Although being known and used as electrode material since decades, in recent years ruthenium-based thin films still gain growing attention as key component in electrochemical applications, such as potentiometric and amperometric sensing [1–3] or energy storage systems (*e.g.*, supercapacitors)[4–6]. The use of ruthenium thin film electrodes in electroanalytical sensing is mainly focused on potentiometric pH sensing. RuO_2 is the most used Ru-based pH sensing material thanks to its Nernstian and super-Nernstian response, which leads to an increased sensitivity toward pH variations compared to the Nernstian response, *i.e.*, a sensitivity larger than 58.3 mV/pH [7,8]. The development of highly sensitive pH sensors is essential for applications in which small variations of pH (*i.e.* 0.1–0.2 units) need to be measured such as in the case of cell cultures [9]. Metallic ruthenium and ruthenium oxide nanoparticles (RuNPs and RuO_2 NPs, respectively) find applications in amperometric sensing thanks to outstanding electrocatalytic properties, which increase the sensitivity and reduce the overpotential of electrodic reactions [10]. The high performances of ruthenium-based NPs modified electrodes have been widely demonstrated in the literature for the detection of several analytes such as toxic chemicals [11], biomolecules [12], drugs [13], antioxidants [14] and amino acids [15].

The microfabrication of Ru^0 and RuO_2 thin film electrodes by coating methods is traditionally performed by different techniques including sputtering, spin-coating, chemical vapor deposition (CVD) and atomic layer deposition [16]. Several of the aforementioned microfabrication methods present drawbacks, such as high costs and complex instrumentation and working environments (*e.g.*, clean room), and the use of masks in case micrometric resolved patterns need to be produced. Ink deposition techniques on the other hand, such as screen printing or inkjet printing, are of great interest for additive manufacturing of electrodes due to their low production and material costs. The conventional

☆ This article is part of a special issue entitled: '11th SMCBS 2023 Workshop' published in Bioelectrochemistry.

* Corresponding author.
E-mail address: andreas.lesch@unibo.it (A. Lesch).

https://doi.org/10.1016/j.bioelechem.2025.108909
Received 7 August 2024; Received in revised form 8 January 2025; Accepted 11 January 2025
Available online 15 January 2025

fabrication of metal and metal oxide thin film electrodes by ink deposition techniques, including drop-casting as a simplified laboratory-scale ink deposition technique, is a multi-step process in which metal (or metal oxide) nanoparticles (MNPs) must first be synthesized by traditional wet methods and purified, before they must be well and stably dispersed in a liquid to prepare an ink with well-defined rheological properties (*e.g.*, viscosity and surface tension) required for the selected ink deposition technique. Once the nanoparticulate ink has been printed or deposited, the MNPs containing liquid layer is first dried and then subjected to a high temperature thermal treatment (generally 300–500 °C depending on the metal) to i.) decompose and evaporate certain ink components (in addition to the solvents often nanoparticle stabilizing agents) and ii.) to sinter the MNPs in order to obtain a conductive and homogeneous metallic thin film [17].

The use of MNP stabilizing agents is required to limit the NP growth during MNP synthesis and to avoid NP aggregation in the inks made for printing. The addition of such compounds increases the complexity of the ink formulation and, with view on electrochemical sensing where the active sensor surface must be pure and clean, of thermal treatments (which by the way are energy intensive and time consuming) to remove all stabilizing agents. In order to reduce the temperatures of post-printing towards room/ambient temperature, several approaches have been suggested, including chemical sintering [18], photonic sintering (*i.e.* flash light irradiation) [19], plasma sintering [20], and Metal Organic Decomposition (MOD) [21,22]. The use of a metal precursor ink instead of a MNPs ink avoids NP aggregation caused issues, such as nozzle clogging during inkjet printing or mesh clogging during screen-printing. Printing a precursor ink and reducing simultaneously or immediately after the precursor into the target is also known as “reactive printing”. For instance, a metal precursor ink can be printed on a substrate and subsequently reduced by a second printed ink layer containing a reducing agent (*e.g.*, $NaBH_4$) [23,24]. This process works well for elements with high reduction potential such as gold or platinum. The use of oxidizing agents and working at air during reactive printing, instead, promotes the formation of metal oxide species. It is therefore possible to tune the oxidation state of the metal by modifying the ink composition. Alternatively, Ru and RuO_2 can be electrodeposited by reduction or oxidation of Ru precursors in electrolytic solution, requiring however a conductive support [25].

One approach that can be seen as a kind of reactive printing is based on the printing of the metal precursor ink on a specific substrate generating micrometer-thin liquid films, which is immediately followed by irradiation using a high-intensity light source (*e.g.*, a xenon flash lamp or UV light) provoking metal precursor conversion and adhesion with complete removal of all other ink components into the gas phase. This method, known as “Print-Light-Synthesis”, was first introduced by Lesch in 2017 to fabricate first Pt nanostructures on ITO coated glass slides [26] and thereafter Ni and NiFe nanocatalysts [27], and Prussian blue thin films [28]. In all of these works a metal precursor ink was inkjet-printed on the substrate and light irradiated with a high intensity xenon flash lamp. Due to the bulky dimensions of the Xe flash lamp it was not possible to perform the irradiation step in real time, thus simultaneously to printing, so the irradiation was carried out subsequently to the inkjet-printing step. In order to perform the two steps of PLS simultaneously, Maiorano, Gianvittorio et al. [29] produced gold thin film electrodes with a single step PLS. Gold (III) chloride as metal precursor was printed and reduced with a UV lamp which was connected to the printhead holder of the inkjet-printer by using a light guide thus irradiating immediately what has been printed just before. Printhead and UV light guide are translated in parallel.

The fabrication of ruthenium-based particles by converting dissolved ruthenium precursors at low temperatures was reported by UV irradiation [30], laser annealing [31] or microwave [32] post-treatments. For instance, Daly et al. have shown that UV light-induced reduction resulted in amorphous RuO_x showing low electrochemical performance compared to NIR irradiated ruthenium 2-ethylhexanoate that resulted in nanocrystalline RuO_x with way better electrochemical performance for the oxygen evolution reaction in alkaline solution [30]. Laser annealing after thermal conversion at 250 °C at air of ruthenium(III) nitrosylacetate increased the RuO_2 film crystallinity and conductivity [31]. To the best of our knowledge, there are only few works concerning the ink deposition for the fabrication of Ru-based patterns, entirely based on printing Ru-based NP inks followed by high temperature treatments [33,34].

Herein we present the simple and low-cost microfabrication of ruthenium oxide (RuO_2) thin film electrodes from a Ru precursor ink at room temperature using Print-Light-Synthesis. It combines the inkjet printing of a ruthenium precursor ink with the immediate UV exposure of the ink film allowing the simultaneous printing and photo-induced conversion of the ruthenium precursor into ruthenium oxide. The fabrication of RuO_2 thin film electrodes and the influence of various printing parameters on the quality of the fabricated RuO_2 patterns will be demonstrated. The as-obtained electrodes will be characterized by X-ray spectroscopy and electron microscope techniques followed by electrochemical characterization. The applicability of the obtained RuO_2 thin film electrodes toward potentiometric sensing for the detection of pH during cell culture and the fabrication and the use of RuO_2-modified inkjet-printed graphene electrodes toward L-cysteine amperometric detection is presented.

2. Materials and methods

2.1. Materials

Ruthenium trichloride (Ru content 45–55 %, $RuCl_3$), sulfuric acid (H_2SO_4), sodium phosphate monobasic, potassium hydroxide (KOH), hydrochloric acid (HCl), acetic acid (CH_3COOH), phosphoric acid (H_3PO_4), boric acid (H_3BO_3) and L-Cysteine were purchased by Sigma-Aldrich. Uric acid (UA) was purchased by Fluka. Potassium nitrate (KNO_3) was purchased by VWR. All compounds were used as received.

A graphene dispersion (graphene ink for inkjet printing with ethyl cellulose in cyclohexanone and terpineol, Sigma-Aldrich), a silver dispersion (30–35 wt% in triethylene glycol monomethyl ether, Sigma Aldrich), and SunTronic UV curing jettable insulator ink (Sigma-Aldrich) were used for inkjet printing of graphene, silver, and a dielectric used as an insulator, respectively. DI water was produced by using an ionic exchange resin filter.

Polyimide (PI) sheets (150 μm thickness) were obtained from Dr. Dietrich Müller GmbH (Germany), microscope glass slides (1 mm thick) from VWR and GC Sigradur K plates from HTW. These three materials were used as substrates for inkjet printing.

2.2. Print-Light-Synthesis of ruthenium and inkjet printing of other sensor components

The Print-Light-Synthesis (PLS) platform was a hybrid system composed of a Fujifilm Dimatix DMP-2831 inkjet printer and an Omnicure S2000 mercury UV lamp (Excelitas). Inkjet-printing was performed by using printheads in the form of cartridges (DMC-11610, piezoelectric actuation, nominal droplet volume 10 pL, 16 individually addressable nozzles), acting as drop-on-demand maskless ink deposition system.

The printhead holder was customized to enable the mounting of a liquid light guide (output diameter 5 mm) that transferred the light emitted by the UV lamp directly onto the substrate with a spot size of ≈5 mm. The 200 Watt UV lamp yielded outputs of up to 30 W cm^{-2} and was herein used with maximum intensity. The position of the light guide output was close to the nozzles of the cartridges and aligned with the printing direction creating a customized PLS head (details in [29]). The cartridge and the UV light were simultaneously translated during PLS, therefore a band of ink was deposited by using between 1 and 16 activated nozzles and immediately irradiated before the next band, after a

perpendicular displacement of the PLS holder, was printed and treated equally. Therefore, a larger pattern was stepwise built up. PLS of RuO_2 was performed by using $RuCl_3$ as metal precursor, which was dissolved in a mixture of water, isopropanol and 1,2-propanediol. The $RuCl_3$ concentration was varied between 0.75 and 15 mg/mL. It must be pointed out that, apart from the ruthenium salt and mixture of solvents, the ink did not contain any other compounds that could have acted for example as stabilizing agent or surfactant. Graphene patterns were printed as conventional electrode material, silver patterns for electrical connections and a UV curable insulator to insulate the silver patterns and to define the electrode area. Inkjet printing parameters, such as piezoelectric actuation pulses and jetting frequencies, were optimized for each ink (Ru precursor, silver, graphene, and insulator inks). Thermal treatments of ink patterns (*e.g.*, graphene and silver) were performed by using a Thermolyne (ThermoFisher scientific) muffle furnace after printing and the UV lamp for photopolymerization of the UV curable insulator ink during printing.

2.3. Characterization of Ru ink and PLS-Ru patterns

UV/Vis absorption spectra of the Ru precursor ink were recorded by using a Hewlett-Packard 8453 diode array spectrophotometer. UV/Vis measurements were carried out as bulk phase measurements for which the ink were filled into Quartz glass containers. Scanning Electron Microscope (SEM) micrographs were recorded by using a Zeiss EP EVO 50 electron microscope. Energy dispersive X-ray spectroscopy (EDS) was recorded by using an Oxford Instruments PentaFET Precision with INCA X-act detector. The software used for the peak analysis was INCA Microanalysis Suite version 4.15 which has an automatic peaks recognition system with internal standard references for the semi-quantitative analysis.

XPS measurements were carried out on an Axis Supra (Kratos Analytical) using the monochromated Kα X-ray line of an Aluminium anode. The pass energy was set to 40 eV with a step size of 0.15 eV. Charge neutralization was used to limit the charging effects, and the data were referenced at 284.8 eV using the aliphatic component of the C1s line.

The resistance of the PLS-RuO_2 patterns was measured by using a Lexman PT1000 multimeter (two-point measurement) or by a collinear four-point-probe measurement system Alessi CPS using osmium probes with a spacing of 1.5875 mm connected to a Keithley 2401 SourceMeter and a collinear four-point probe device with 1 mm separated solid tungsten carbide probes (Jandel Engineering) connected to a Keysight Precision Source/Measure Unit B2902B.

Optical microscope analysis and pictures were performed by using a Dino-Lite digital microscope coupled with a DinoCapture software.

2.4. Electrochemical measurements

Electrochemical measurements were performed by using conventional electrochemical workstations, herein a CHI-900b (CH Instruments) and a CompactStat (Ivium Technologies). Voltammetric measurements were carried out in a three-electrode cell configuration by using PLS-RuO_2 electrodes or electrodes for comparison as working electrode (WE), a platinum wire as counter electrode (CE) and a Ag/AgCl (1 M KCl) electrode as reference electrode (RE). All potentials herein are referred to this RE. Currents recorded in the voltammograms were expressed as geometric current densities J_{geom}. Potentiometric measurements were carried out in a two-electrode cell configuration by using PLS-RuO_2 electrodes as WE and a Ag/AgCl (1 M KCl) electrode as RE. To perform potentiometric measurements the Open-Circuit-Potential E_{OCP} was measured up to 600 s. Buffered solutions for potentiometric measurements were prepared by using a universal buffer solution (0.1 M KNO_3, 0.01 M H_3PO_4, 0.01 M CH_3COOH, 0.01 M H_3BO_3) and the pH of each prepared solution was measured during the preparation by using an AMEL Instrument 338 pH meter.

2.5. Cell culture and pH measurements

CAL 27 epithelial cells (ATCC) were cultured in high glucose DMEM medium (Dulbecco's Modified Eagle Medium, Microgem, PMSTVMSV) supplemented with 20 % (vol/vol) Fetal Bovine Serum (South America, Microtech, RM10432), 2 mM L-glutamine, 50 U/mL penicillin and 50 μM streptomycin. After seeding approximately 2.7 millions of cells in 11 mL of complete medium, fresh growing medium was provided at the beginning of pH monitoring, which started 24 h from cell seeding. CAL 27 cells were cultured in 10 cm diameter Petri dishes, reaching a cell confluency of approximatively 70 % after 48 h. For the cell cultures pH monitoring each RuO_2 pH sensor was calibrated with three buffered solutions at pH 6, 7 and 8 (three-point calibration). Buffered solutions for the calibration were prepared by using the cell culture media and adjusting the pH value with diluted HCl. The pH of each prepared solution was measured by using an XS Instruments pH 7 portable pH meter.

3. Results and discussion

3.1. Print-Light-Synthesis of ruthenium oxide

For Print-Light-Synthesis (PLS) of RuO_2, a thin liquid layer of ruthenium precursor ink was deposited and the dissolved Ru salt was treated by photochemical activation. To successfully perform PLS for RuO_2 patterning, printability of the Ru precursor ink must be achieved, and the photo-induced conversion must be realized. For the evaluation of the jettability of the ink, the Ohnesorge number (*Oh*) was used as numeric indicator [35]. The reciprocal of *Oh* has been introduced in the literature as the dimensionless *Z* number defined as $Z = Oh^{-1} = (\gamma \times \rho \times d)^{0.5}/\eta$, where γ, η, and ρ are the surface tension, viscosity, and density of the ink, respectively. The quantity d represents a characteristic length, which is the diameter of the nozzle orifice, *i.e.*, 21.5 μm. The calculated *Z* value was equal to 6.49 and was therefore within printability range of $1 < Z < 10$ [35]. The Ru precursor ink was inkjet-printed obtaining stable and reproducible droplets with an average volume of (11.9 ± 0.2) pL (3 droplets average). The photochemical conversion of a metallic precursor can be the result of the formation of reactive radicalic species [36]. The photochemical reduction of dissolved $RuCl_3$ by using irradiation with light of different wavelengths, irradiation times, and intensities has been widely studied and the mechanistic pathways under various experimental conditions are well established [37–40]. Alcohols (*i.e.*, isopropanol) can also get involved in the Ru^{3+} photoreduction mechanism by acting as sacrificial electron donors [37]. In this work, a UV mercury lamp has been used as light source and Fig. 1b shows the emission spectra of the lamp while Fig. 1a shows the absorption spectra of the used Ru precursor ink before and after irradiation.

As it can be seen from Fig. 1a, the Ru precursor ink, placed as bulky solution phase in a Quartz glass container, showed one main broad absorption wave at around 339 nm, which overlapped well with the emission wavelengths of the mercury UV lamp, and a second absorption wave at about 500 nm. The pure solvent mixture, thus in absence of dissolved $RuCl_3$, showed negligible absorption in the UV lamp emission region. The presence of dissolved $RuCl_3$ in the solvent mixture therefore increased the UV absorption capacity of the ink. The photochemical reactivity of the Ru precursor ink toward UV irradiation was demonstrated by irradiating 1.0 mL of the Ru precursor ink with the UV lamp for 600 s. After UV irradiation the colour of the ink changed (Supporting Information SI, SI-1) indicating that a photochemical process took place with conversion of the Ru precursor. As it can be seen from the absorption spectrum in Fig. 1a, the irradiated Ru precursor ink (blue line) showed the decrease in the intensity of the absorption at 339 nm, making furthermore the peak narrower, and the disappearance of the second absorption peak at 500 nm, indicating both a decrease of the dissolved $RuCl_3$ concentration in the ink, most likely caused by the photochemical conversion of the Ru precursor [41].

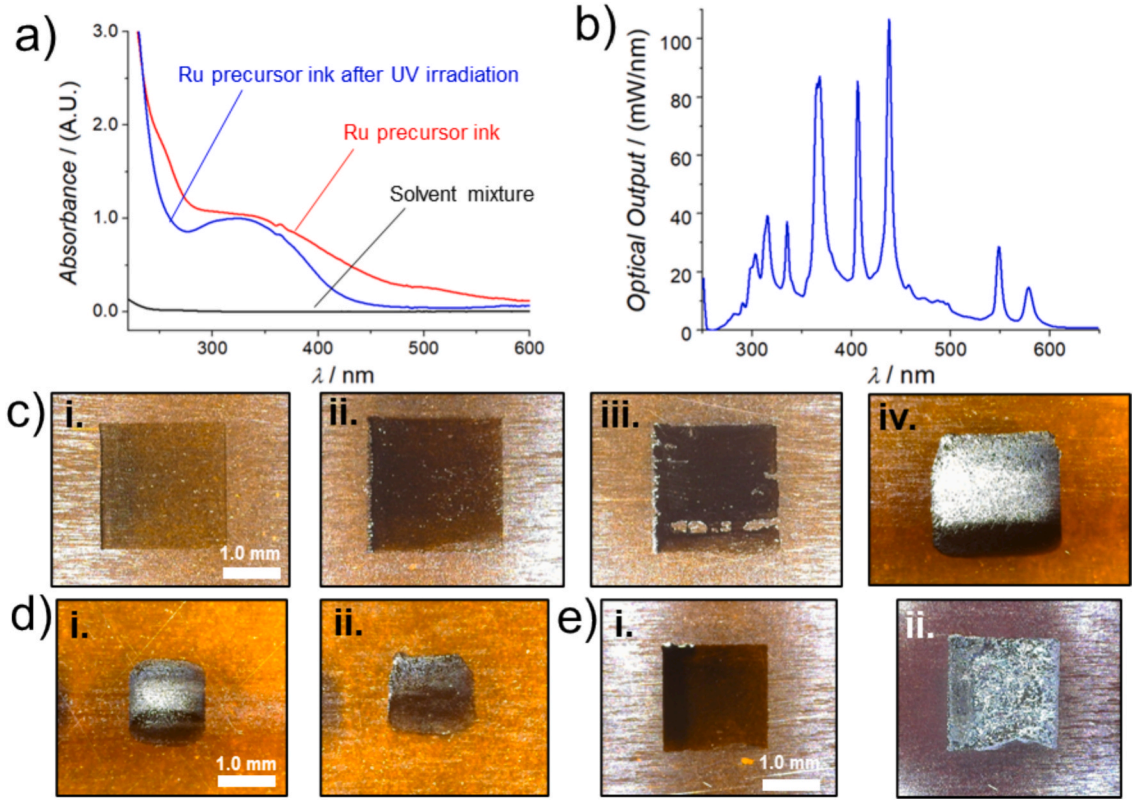

Fig. 1. (a) UV/Vis absorption spectra of the Ru precursor ink (red curve), UV irradiated Ru precursor ink (blue) and Ru-free ink (black). (b) Emission spectrum of the UV mercury lamp. (c) Optical micrographs of Ru-based patterns of 4 mm^2 area on PI as obtained by PLS using 15 mg/mL Ru precursor ink and different dpi numbers: i. 1270 dpi (22.46 $\mu g_{Ru}/cm^2$; resistance = infinite), ii. 1693 dpi (40.03 $\mu g_{Ru}/cm^2$; resistance = 132 MΩ), iii. 2540 dpi (85.81 $\mu g_{Ru}/cm^2$; resistance = 600 kΩ) and iv. 5080 dpi (243.85 μgRu/cm^2; resistance = 25 Ω). (d) Optical micrographs of Ru-based patterns of 1 mm^2 area on PI prepared by PLS using the same dpi number (5080 dpi) but different Ru precursor ink concentrations of i. 15 mg/mL (191.82 $\mu g_{Ru}/cm^2$, resistance = 132 Ω) and ii. 7.6 mg/mL (105.32 $\mu g_{Ru}/cm^2$, resistance = 1200 Ω). e) Optical micrographs of Ru-based patterns inkjet-printed with 15 mg/mL Ru precursor ink on PI with 5080 dpi (369.32 $\mu g_{Ru}/cm^2$), before (i., resistance = infinite) and after (ii., resistance = infinite) thermal treatment at 400 °C for 30 min using a muffle oven (2 °C/min heating ramp).

During PLS, where micrometer thin ink volumes are irradiated, the degree of the conversion of the Ru precursor is strongly dependent on the printing parameters (*e.g.*, dpi number or UV light intensity). The precursor conversion must be rapid in order to be complete before the ink solvents have entirely evaporated. Otherwise, one would only deposit $RuCl_3$, at least to a large extend. The dpi number is an essential parameter in inkjet printing and represents the number of droplets deposited per inch on the substrate. This parameter allows for instance to control the metal precursor loading deposited on the substrate (when using a fixed precursor concentration in the ink). Another parameter that can be controlled is the printhead velocity that determines indirectly the exposition time of the ink thin film by the UV light, which translates together with the printhead. The effect of the dpi number during Ru PLS was therefore priorly investigated as one of the key parameters for inkjet printing Ru patterns on PI (Fig. 1c). On the one hand, printing with increasing dpi numbers up to 5080 dpi increased the Ru loadings. On the other hand, increasing light exposition times per area was achieved when fixing the time between to deposited droplets and reducing their distance with increasing dpi. With 5080 dpi, the obtained inkjet-printed Ru ink patterns appeared metallic-like, conductive (resistance = 25 Ω) and insoluble in water indicating that the conversion of $RuCl_3$ was complete and that the PLS-Ru ink pattern was well adhered. Printing with a lower dpi number (*i.e.*, <5080 dpi) reduced the Ru loading and UV light exposition times per substrate area. As a consequence, the as-obtained PLS-Ru ink patterns appeared liquid and soluble in water indicating therefore that the conversion of $RuCl_3$ was incomplete. In an alternative approach, the Ru loading on the substrate was changed by adjusting the Ru precursor concentration in the ink while keeping the dpi number constant. Fig. 1d shows an example of two PLS-Ru patterns with the same dpi number but with two different Ru precursor ink concentrations. The resistance of the RuO_2 film with lower Ru loading, *i.e.*, 105 $\mu g_{Ru}/cm^2$, was 10 times higher (1200 Ω) in respect to a RuO_2 film with nearly double Ru loading, *i.e.*, 192 $\mu g_{Ru}/cm^2$ (132 Ω). For comparison, a traditional thermal treatment of an inkjet-printed Ru precursor ink pattern was performed at air, thus without UV light irradiation. 400 °C was selected as temperature, which on the one hand is the maximum thermal process temperature that PI can withstand. On the other hand, it was theoretically the maximum temperature that was generated in PI during PLS by light absorption and local heat generation, because no thermal PI degradation was observed during PLS. Fig. 1**e** shows that the Ru precursor was converted into a solid phase that however was not conductive. Furthermore, RuO_2 detached easily from the substrate.

Fig. 2a (i.–iii.) shows representative SEM micrographs of PLS Ru ink samples, inkjet-printed with three different dpi numbers. As it can be seen, the PLS Ru films present a typical solid structure made of Ru-based plates with average lateral dimensions of about 5–10 μm that appear disconnected by cracks. However, the conductivity measurements demonstrate that globally conductive films were obtained by PLS. The highest Ru loading, *i.e.*, 244 $\mu g_{Ru}/cm^2$, Fig. 2a-iii, showed less cracks. Notably, the resistance of the RuO_2 films with that high loading was 24,000 times lower (25 Ω) compared with a three times lower Ru loading, *i.e.*, 86 $\mu g_{Ru}/cm^2$ (600 kΩ). The SEM micrographs of the RuO_2 film printed with 2540 dpi shows some brighter zones while the RuO_2 film with just 1693 dpi shows some greyish spots. The latter was most likely due to unconverted $RuCl_3$ and could there therefore represent

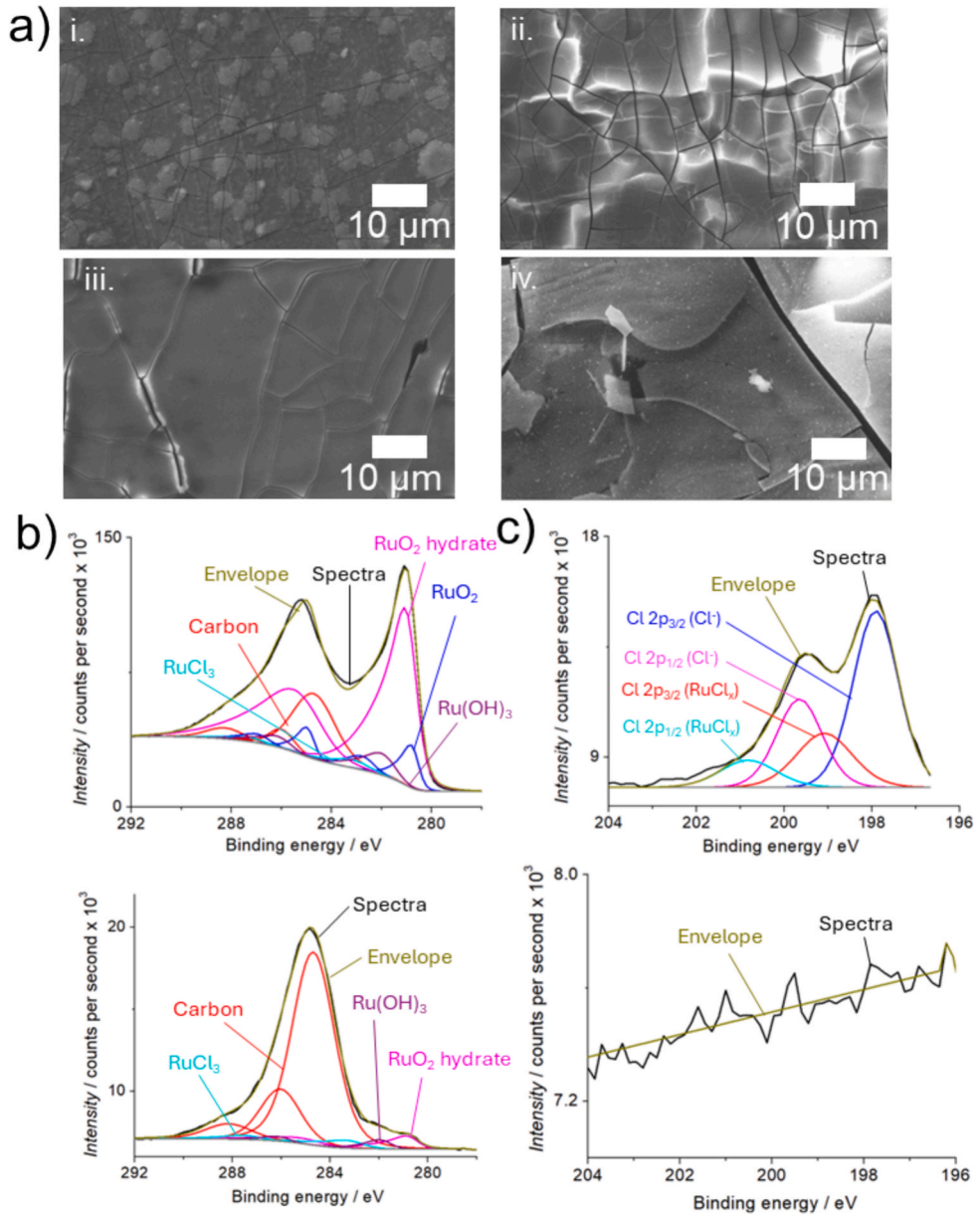

Fig. 2. (a) Representative SEM micrographs (5,000× magnification) of Ru precursor ink patterns inkjet-printed on PI by PLS using different dpi numbers and treatment methods: i. 1693 dpi (40.03 $\mu g_{Ru}/cm^2$; PLS; resistance = 132 MΩ), ii. 2540 dpi (85.81 $\mu g_{Ru}/cm^2$; PLS; resistance = 600 kΩ), iii. 5080 dpi (243.85 $\mu g_{Ru}/cm^2$; PLS; resistance = 25 Ω) and iv. 5080 dpi (369.32 $\mu g_{Ru}/cm^2$; thermally treated in a muffle furnace at 400°C for 30 min; resistance = infinite), (b) XPS spectra of Ru 3d peaks with fitted curves for PLS-RuO_2 (upper panel) and thermally obtained RuO_2 (lower panel) on PI. (c) XPS spectra of Cl 2p peaks with fitted curves for PLS-RuO_2 (upper panel) and thermally obtained RuO_2 (lower panel) on PI.

precursor salt residues. The thermally obtained RuO_2 film (Fig. 2a-iv) shows more extended cracks and many tiny bright spots, indicating clearly a different material conversion process. As a result of the cracks, the thermally obtained film appeared non-conductive.

The EDX spectroscopy analysis (SI-2) performed on each of these samples revealed that the weight percentage of Ru in the pattern, which was inkjet-printed with 5080 dpi, was 96.5 % with a residual chlorine weight percentage of 3.5 %. This was the highest degree of conversion of $RuCl_3$ obtained using the PLS platform of this work. The initial Ru content in weight percentage in the precursor was 45–55 %. Inkjet-printed patterns with 2540 and 1693 dpi instead showed lower Ru weight percentages of 72.8 % and 66.7 %, respectively. These quantitative numbers confirm that the degree of conversion of $RuCl_3$ decreases as the dpi number decreases. This suggests that the PLS process of Ru depends on the loading of dissolved precursor in the ink on the substrate and the light exposure time in order to absorb sufficiently UV irradiation and initiate the conversion processes.

In other recently studied PLS processes the mechanism of the metal precursor conversion has been demonstrated to be a hybrid photochemical and photothermal reduction process in case the irradiated system contains a so-called light-to-heat absorption layer [26,29]. The photo-thermal reduction is possible when the irradiated ink thin film and/or the substrate below absorb irradiation and heat up. When reaching several hundred degrees Celsius thermal decomposition of the metal precursor into pure metal can set it. In the case of $RuCl_3$, the photochemical reduction during PLS might promote the formation of metallic Ru particles, while the photothermal process could lead to Ru particle sintering and the formation of RuO_2, because the process generates elevated temperatures and takes place in the presence of oxygen [42]. The local heat generation during PLS shows moreover the

advantage to facilitate the evaporation of the ink solvents. The ink thin film heating can be a result of i) the substrate heating by UV absorption or ii) the ink thin film heating itself by UV absorption. In fact, PI absorbs very well UV irradiation (SI-4) and generates high temperatures (300–400 °C). On the contrary, on substrates which possess a higher heat dissipation capacity (like glassy carbon) or very low absorption (like glass) the Ru precursor conversion was inefficient as the ink film remained still liquid and unconverted (SI-5). According to general literature, the thermal elimination of chlorine with the formation of RuO_2 is complete between 450 and 800 °C (depending on the O_2 partial pressure) [42,43]. Because temperatures near or above 400 °C have not been reached during PLS (because no degradation of PI was observed, as there was neither a change of colour nor a PI deformation, which takes place above 400 °C and which was seen with the thermal treatment), based on the preliminary UV irradiation tests, and considering general literature, we assume that photochemical processes contributed.

XPS analyses were then performed on both PLS-Ru (244 $\mu g_{Ru}/cm^2$, 5080 dpi) and thermally generated Ru patterns (400 °C) to confirm the identity of the obtained Ru species on PI and to compare both Ru precursor conversion methods (more detailed XPS spectra in SI-3). The Ru 3d signal (Fig. 2b) was used to confirm the identity of the Ru phase while the Cl 2p signal (Fig. 2c) was used to evaluate the amount of chlorine that remained after both processes. The Cl content was related to the amount of Ru to evaluate the degree of conversion of the Ru precursor. The identification of Ru species on a carbon-based support by XPS is challenging due to the strong overlap between the Ru 3d and C 1 s signals [44]. Herein, peak fitting was adopted from Morgan et al. [44] and showed that the dominant Ru species in PLS-Ru were RuO_2 and RuO_2 hydrate with a small amount of Ru^{3+}, which remained as $Ru(OH)_3$ from $RuCl_3$ hydrolysis and minor non hydrated residuals of $RuCl_3$. The presence of residual Cl after PLS was confirmed by the presence of a weak Cl 2p signal, in agreement with the EDX analysis (vide supra). The calculated atomic ratio between Ru and Cl in the PLS-RuO_2 pattern was equal to 19 while for a pure $RuCl_3$ phase it is equal to 0.33 [44,45]. This evidence confirms a nearly complete conversion (≈97 %) of $RuCl_3$ into RuO_2 during PLS.

On the contrary, for the thermally treated Ru ink pattern, the Ru 3d signal shows a dominant presence of carbon species, which might have been caused by the starting degradation of the polyimide substrate at 400 °C that could have contaminated the RuO_2 surface, causing, besides the previously discussed cracks, the low or absent electrode conductivity. The fitted curves for Ru phases confirmed the presence of hydrous and anhydrous RuO_2. The Cl 2p signal was not present in the thermally treated Ru ink sample thus indicating the nearly complete or complete thermal conversion of $RuCl_3$ into RuO_2. For both methods, no metallic Ru was detected. The XPS analyses, in addition to the conductivity measurements, demonstrate that with PLS a functioning RuO_2 electrode on polyimide can be constructed at ambient conditions while with the traditional thermal method only a non-conductive, most likely contaminated, pattern of RuO_2 fragments was obtained. Hence, PLS has major advantages for printing flexible devices with PI sheets as substrates.

3.2. Ruthenium oxide thin film electrodes by Print-Light-Synthesis

Print-Light-Synthesis was employed on the one hand to fabricate RuO_2 thin film electrodes on PI and on the other hand RuO_2 NP-modified inkjet-printed graphene electrodes. In the former case a complete conductive RuO_2 electrode was prepared applying the highest dpi number with high Ru precursor concentration to result in high Ru loadings. In the latter case individual RuO_2 particles on graphene were generated with the same high dpi number but a with a 10 times lower Ru precursor concentration in the ink, obtaining therefore a lower Ru loading and separated RuO_2 particles on the graphene surface. Graphene also absorbs part of the UV light so that the graphene layer can act as an additional or alternative light-to-heat absorption layer compared the bare PI [27]. Ruthenium oxide thin film electrodes on PI were prepared with one or two deposited Ru precursor ink layers doubling in this way the precursor loading. One printed Ru precursor layer resulted in Ru loadings between 90 and 145 $\mu g/cm^2$ (depending on the printing resolution) with a resistance of 133 Ω (141.4 $\mu g_{Ru}/cm^2$), while RuO_2 thin films inkjet printed with two ink layers showed a Ru loading of about 200–220 $\mu g/cm^2$ and a resistance of just 2.34 Ω (211.4 $\mu g_{Ru}/cm^2$). It was observed that the second printing passage, *i.e.*, the second layer printing, not only increases the Ru loading, but also supports the covering of cracks, holes and imperfections that remained from the first printing passage, thus increasing the thin film conductivity.

A fully inkjet-printed RuO_2 working electrode is shown in Fig. 3a. The Ru film was made by PLS and overlapped slightly with a previously inkjet-printed silver pattern used for electrical connection and electrical

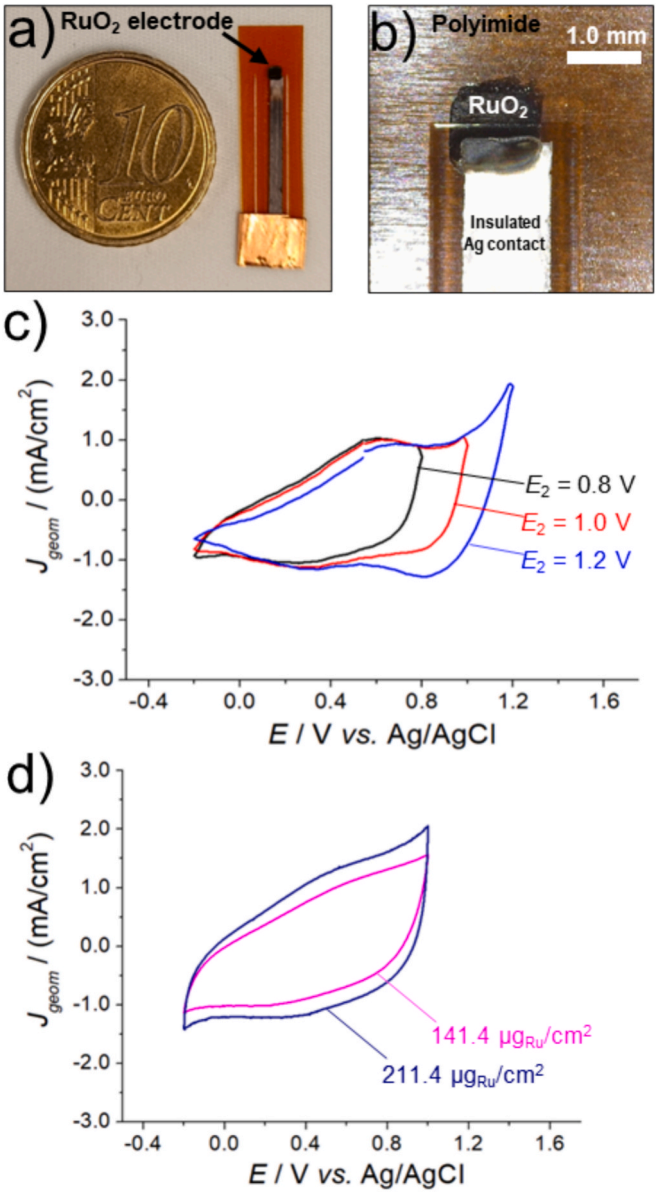

Fig. 3. Fully inkjet-printed Ru-based working electrode, full scale picture (a) and digital microscope picture, 50× magnification (b). c) Electrochemical characterization of a PLS-RuO_2 thin film electrode (92.22 $\mu g_{Ru}/cm^2$, geometric WE area 0.99 mm^2) by CV in 0.5 M H_2SO_4, scan rate 25 mV/s, 2nd cycle, different upper vertex potentials. d) Cyclic voltammograms recorded using two PLS-RuO_2 film electrodes with two different inkjet-printed Ru ink layers, 1 layer (141.4 $\mu g_{Ru}/cm^2$; pink curve) and 2 layers (211.4 $\mu g_{Ru}/cm^2$; blue curve) in 0.5 M H_2SO_4, scan rate 25 mV/s, 5th cycle.

contact (the electrical silver contact was mechanically stabilized with a Cu tape). Finally, a dielectric layer was inkjet printed on the sensor to insulate the silver and protect it from the electrolyte solution during electrochemical measurements. The RuO_2 conductive patterns that remained exposed to the electrolyte solution had areas between 0.6 and 0.9 mm^2 depending on the final printing parameters (Fig. 3b). The PLS of RuO_2-modified graphene electrodes (Fig. 4a) was performed by inkjet-printing a single layer of Ru precursor ink on graphene in order to cover a squared active graphene area of 4 mm^2 with a low Ru loading of 15 $\mu g/cm^2$.

3.3. *Electrochemical behaviour of PLS-RuO_2 thin film electrodes and PLS RuO_2 NP-modified graphene electrodes*

The electrochemical characterization of the RuO_2 thin film electrodes was performed with cyclic voltammetry (CV) in 0.5 M H_2SO_4. The WE potential was cycled between −0.2 V (lower vertex potential) and a variable higher vertex potential E_2. The CVs in Fig. 3c show significant capacitive currents due to the presence of the RuO_2 film. A small anodic peak is seen at about 0.6 V and a small reduction peak at about 0.3 V. When E_2 was set to 1.2 V a small further anodic peak is seen just above 1 V resulting however in a clear reduction peak at about 0.83 V. The reduction peak at 0.83 V can be ascribed to the reduction of the as formed $Ru^{(VIII)}$oxide into the $Ru^{(VII)}$oxyanion [46]. Near 1.2 V the oxygen evolution reaction (OER) most likely set in, which, however, was not in the focus of the present work.

The effect of the number of inkjet-printed Ru precursor ink layers on the electrochemical behaviour of the RuO_2 thin film electrodes was thereafter investigated. Fig. 3d shows two voltammograms recorded with two PLS-RuO_2 film electrodes inkjet-printed with two different Ru precursor ink layers. The single print layer PLS-RuO_2 film electrode possessed a Ru loading of 141.4 $\mu g/cm^2$ while the two printed ink layers PLS-RuO_2 electrode had a Ru loading of about 211.4 $\mu g/cm^2$. The ratio between the Ru loading of these two electrodes was therefore 1.5. Considering the current values recorded for both electrodes at 0.5 V where a shoulder is present in each curve (which can be ascribed to the oxidation of Ru^0 to Ru_2O_3 in acid environment [47]), the ratio between those current values was equal to 1.44 which is very close to the ratio

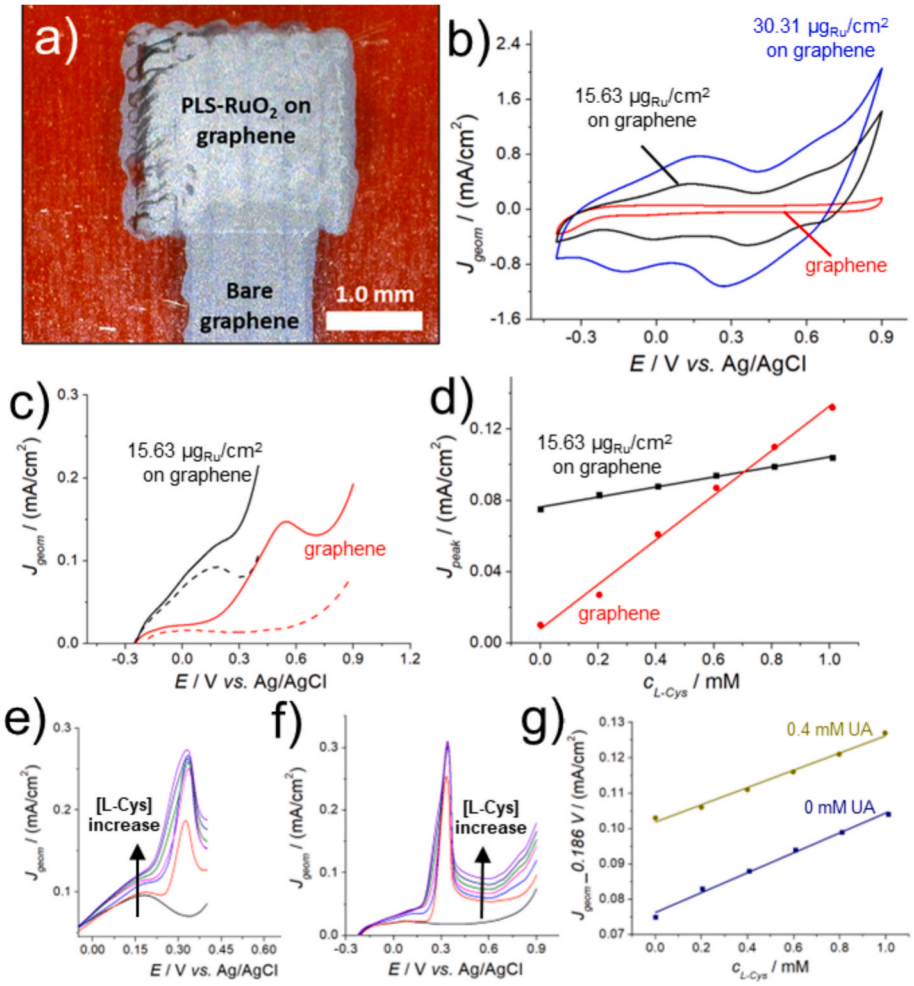

Fig. 4. (a) PLS-RuO_2-modified graphene working electrode (2 mm × 2 mm pattern), digital microscope picture, 50× magnification, before printing the insulation layer on bare graphene. (b) Electrochemical characterization of bare graphene (red curve) and 2× PLS-RuO_2-modified graphene (15.63 $\mu g_{Ru}/cm^2$ (black) and 30.31 $\mu g_{Ru}/cm^2$ (blue), respectively; geometric WE area 0.04 cm^2) by CV in 0.1 M phosphate buffer (pH 7), scan rate 100 mV/s, 5th cycle. (c) Linear-sweep voltammograms recorded using bare graphene (red curves) and the PLS-RuO_2-modified graphene (black) electrodes in the absence (dashed lines) and in the presence of 1.0 mM of L-cysteine (full lines) in 0.1 M phosphate buffer (pH 7), scan rate 25 mV/s. (d) Calibration graphs for L-cysteine obtained using a bare graphene (red; slope = 0.125 mA/(cm^2 mM); R^2 = 0.992) and a PLS-RuO_2-modified graphene WE (black; slope = 0.028 mA/(cm^2 mM); R^2 = 0.992). (e) Linear-sweep voltammograms recorded using a PLS-RuO_2 modified graphene electrode (15.63 $\mu g_{Ru}/cm^2$) in the presence of 0.4 mM UA and with increasing concentration of L-Cysteine. (f) Linear-sweep voltammograms recorded using a bare graphene electrode in the presence of 0.4 mM UA and with increasing concentration of L-Cysteine. (g) Calibration graphs for L-Cysteine obtained by using a PLS-RuO_2 modified graphene electrode (15.63 $\mu g_{Ru}/cm^2$) in the presence (yellow line; slope = (0.024 ± 0.001) mA/(cm^2 mM)) and in the absence (dark-blue line; slope = (0.028 ± 0.001) mA/(cm^2 mM)) of 0.4 mM of UA.

between the respective Ru loadings. This suggests that increasing the Ru loading increases the real surface area of the Ru film electrodes. Therefore, thanks to the variety of controllable printing parameters, *e.g.*, by varying the number of inkjet-printed Ru layers and dpi numbers, the capacitance and thus the electrochemical behaviour of PLS-RuO_2 film electrodes can be tuned. Thereafter, the electrochemical performance of the PLS-RuO_2-modified inkjet-printed graphene electrodes was evaluated (Fig. 4b-g) where individual RuO_2 particles improve the sensing characteristics of graphene by means of electrocatalysis.

The voltammetric characterization of a PLS-RuO_2 NP-modified graphene electrode in 0.1 M phosphate buffer (pH 7) reveals the characteristic redox peaks of the Ru system [48] (Fig. 4b), while the CV of the bare graphene electrode demonstrates only low capacitive currents. The capacitive current contribution given by the RuO_2 particles film was tuned by varying the inkjet-printed Ru loading on the graphene surface, as seen for 15.63 $\mu g_{Ru}/cm^2$ and 30.31 $\mu g_{Ru}/cm^2$ in Fig. 4b. In terms of electroanalytical applications, the presence of RuO_2 on graphene resulted in an electrocatalytic effect toward the detection of 1.0 mM L-cysteine with an anodic peak potential shift of −362 mV (Fig. 4c) in 0.1 M phosphate buffer (pH 7). It must be noted that the sensitivity of the RuO_2 NP-modified graphene electrode was lower than bare graphene due to the higher contributions of capacitive currents in the presence of ruthenium (Fig. 4d; even at lower scan rates, results not shown). However, the PLS-RuO_2 NP-modified graphene electrode showed a good linearity toward L-cysteine detection and a good limit of detection (LOD = 100 μM). Considering that the L-Cysteine concentration level in real samples, such as human serum, is between 240 and 360 μM [49] the limit of detection and the linearity range of the PLS-RuO_2 modified sensors are suitable for performing L-Cysteine amperometric detection. The main advantage of using PLS-RuO_2 modified electrodes is given by the electrocatalytic effect of RuO_2 [50], which allows L-cysteine detection at reduced overpotentials reducing the risk of interferent oxidation phenomena at the electrode surface caused by other oxidizable species which could be present in real samples, such as uric acid (UA). This was demonstrated by performing the L-Cysteine amperometric detection in the presence of 0.4 mM UA, which is its normal concentration in human serum [51]. The results shown in Fig. 4e illustrate that the presence of RuO_2 on graphene allow a selective response to L-Cysteine at a potential of 0.186 V vs Ag/AgCl, because for UA no electrocatalytical effect was observed separated the two signals efficiently. This behaviour was not achieved on a bare graphene electrode, where it was not possible to distinguish the two oxidation processes and to obtain a proportional response to L-Cysteine (Fig. 4f). The response of the RuO_2 modified graphene sensor was found to be linear in the presence of UA and the obtained sensitivity was very close to the one obtained in the absence of UA as interferant (Fig. 4g), demonstrating that the graphene modification with PLS-RuO_2 allows L-Cysteine detection avoiding the effect of other interferent oxidizable species.

3.4. PLS-RuO_2 thin film electrodes as potentiometric pH sensors

The behaviour of PLS-RuO_2 thin film electrodes toward potentiometric pH sensing was investigated by using two PLS-RuO_2 thin film electrodes with two different Ru loadings, *i.e.*, 112.51 $\mu g/cm^2$ and 206.33 $\mu g/cm^2$, respectively. The pH measurements were performed at 21 °C using universal buffer solutions in a pH range from 2 to 12 units. The E_{OCP} value for each measurement was sampled at the time of 600 s in order to reach the maximum signal stabilization. Fig. 5 shows the results obtained for pH sensing by using the PLS-RuO_2 electrode with the higher Ru loading. Upon change of pH the PLS pH sensor responded rather quickly, apart from the more acidic solutions where longer times were required to obtain the constant E_{OCP}. (Fig. 5a).

The calibration graph in Fig. 5b shows that the PLS-RuO_2 film electrode inkjet printed with two Ru precursor ink layers (206.33 $\mu g_{Ru}/cm^2$) displayed a linear response ($R^2 = 0.999$) toward pH variations with an average Nernstian slope of (57.9 ± 0.7) mV/decade (mean of 3 repeated

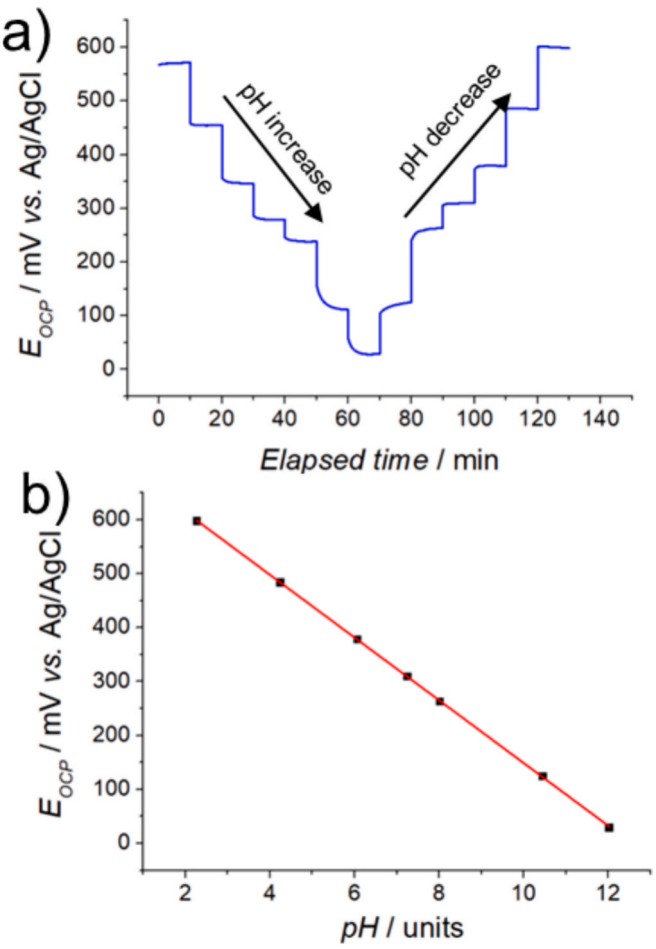

Fig. 5. Performance of a PLS-RuO_2 thin film electrode (206.33 $\mu g_{Ru}/cm^2$) for potentiometric pH sensing, E_{OCP} measurements as a function of time (a) and resulting calibration graph (b) with slope = −58.2 mV/unit ($R^2 = 0.999$).

measurements) in respect to the theoretical slope of 58.3 mV/decade at 21 °C. Thus, the PLS pH sensor response corresponded to the theoretical value. In general, the Nernstian behaviour of ruthenium oxide as a function of pH can be ascribed to the presence of equilibrium reactions between $Ru^{(IV)}$ and other Ru oxide species (mainly $Ru^{(III)}$) which can establish at the RuO_2 electrode surface [52]. The PLS-RuO_2 electrode inkjet printed with a single Ru ink layer (112.51 $\mu g_{Ru}/cm^2$) also showed a linear response as a function of pH but with an infra-Nernstian average slope of (53.4 ± 2.5) mV/decade (mean of 3 repeated measurements). However, the PLS-RuO_2 film electrodes inkjet printed with two Ru ink layers (206.33 $\mu g_{Ru}/cm^2$) showed a better signal stabilization in 10 min of the E_{OCP} for each tested pH value. The difference between the two performances can be ascribed to the different thicknesses of the RuO_2 thin film in the two PLS-RuO_2 electrodes. A PLS-RuO_2 electrode inkjet-printed with a single layer of precursor ink possess lower thickness respect to a PLS-RuO_2 electrode inkjet-printed with two layers of precursor ink. As the RuO_2 film thickness increases the sensitivity of the sensor increases too leading to better sensing performances toward potentiometric pH sensing [8]. This behaviour confirms that varying the number of printed RuO_2 layers (and consequently the Ru loading and the film thickness) reveals a good way to tune the potentiometric sensing performances of the PLS-RuO_2 electrodes.

3.5. Potentiometric pH monitoring of CAL-27 cells cultures using PLS-RuO_2 thin film electrodes

To demonstrate the applicability of the PLS-RuO_2 thin film electrodes

for pH measurements of samples of high analytical interest, the acidification of the culture medium of a CAL 27 cell culture was investigated. CAL 27 is a head-neck cancer cell line. Usually, pH modification of the cell growing medium is observed for any cell type as a consequence of cell growth, mainly due to catabolic consumption of glucose by the cells. Glycolytic partial oxidation of glucose to pyruvate is a major source of ATP at high glucose growing conditions. Pyruvate conversion to lactate and its release in the growing medium is the main cause of medium acidification over culturing time. Another cause of the acidification of growing medium in laboratory conditions could be the presence of cancer tissues that leads to a lactate release by cells. This local acidification of cell surroundings by lactate has been described to be determinant in cancer cell growth and resistance to therapy [53]. As a consequence, numerous analytical methods for pH and lactate monitoring in cells cultures [54] or *in vivo* and real tissues have been described and have biomedical and bioanalytical applications. In fact, cell culture media often contain pH indicators to demonstrate a colour change during cell culture acidification. The potentiometric pH measurements in CAL 27 cell culture were performed twice during the growth process separated by 24 h using a PLS-RuO_2 thin film electrode inkjet-printed with two layers of Ru precursor ink (206.33 $\mu g_{Ru}/cm^2$). In order to avoid disturbance of the cell culture and potential risk of contamination by immersion of the electrodes into the culture, 0.9 mL of the medium was taken and placed into a small 3D-printed 2-electrode electrochemical cell, specifically designed and printed on demand for the scope of this work (Scheme 1a and c). The measurement cell was kept inside the microincubator during the measurement in order to maintain the same conditions, in particular the CO_2 level, as during cell culture. For such measurements it is indeed essential to work under constant CO_2 pressures, as the CO_2 pressure regulates and/or influences the pH of the solutions under investigation. The experimental setup of the microincubator with customized 3D measurement cell is illustrated in Scheme 1b.

The pH values measured at each time were extrapolated from the average calibration graph obtained by the mean of 3 replicated calibrations recorded by using three PLS-RuO_2 sensors in the cell culture medium with adjusted pH and controlled atmosphere (Fig. 6a). The sensor sensitivity was substantially reduced in the culture media compared to simple aqueous buffer solutions. This demonstrates that besides considering the atmosphere, calibration graphs must be obtained in proper media. RuO_2 is a redox material that can undergo transformations in complex matrices affecting the sensitivity. This is an effect that all metal oxide based pH sensors experience. Glass-based pH electrodes are not affected, but difficult to miniaturize and to fabricate as disposable sensors. The PLS pH sensor responses were compared with those of the commercial pH meter as a control. For instance, at time point zero the measured pH with the PLS-RuO_2 electrode was (7.54 ± 0.15) pH units (mean of 3 sensors) whereas it was (7.51 ± 0.02) pH units for the commercial glass pH electrode (mean of 3 repeated measurements). Fig. 6b illustrates the results obtained for CAL 27 pH. A pH acidification of 0.80 units was detected after 24 h as a consequence of the cell growth. The PLS-RuO_2 thin film electrodes showed a good signal stabilization during the measurement in cell culture medium confirming their applicability for real samples potentiometric pH measurements and offering an alternative low cost, miniaturized, and fast solution to traditional pH measurement systems (*i.e.*, glass electrodes). The use of the microcell eliminated the risk to contaminate the cell culture and keeps the measurement volume very low. As a potential application of the PLS pH sensor, monitoring the pH without dissolved indicator (that affects solution colour) can be realized.

4. Conclusions

To conclude, PLS of Ru-based electrodes for bioelectroanalytical sensing applications was presented. A Ru precursor ink was inkjet-printed and coupled with its simultaneous photo-induced reduction to generate homogeneous RuO_2 thin films in one step. The Ru precursor ink did not require stabilizing agents. Inkjet printing generated micrometer-thin reaction volumes in which dissolved $RuCl_3$ was converted into $Ru^{(IV)}$oxide, most likely by a hybrid photochemical/photothermal process. The Ru^{3+} was converted into RuO_2, and all other ink components were removed in the gas phase. The controlled deposition of variable quantities of Ru (100–200 $\mu g_{Ru}/cm^2$) was achieved by optimizing PLS parameters (*e.g.*, dpi number, ink concentration, number of inkjet-printed layers and UV light intensity) and demonstrate the high sustainability of PLS in using small amounts of precious metals without

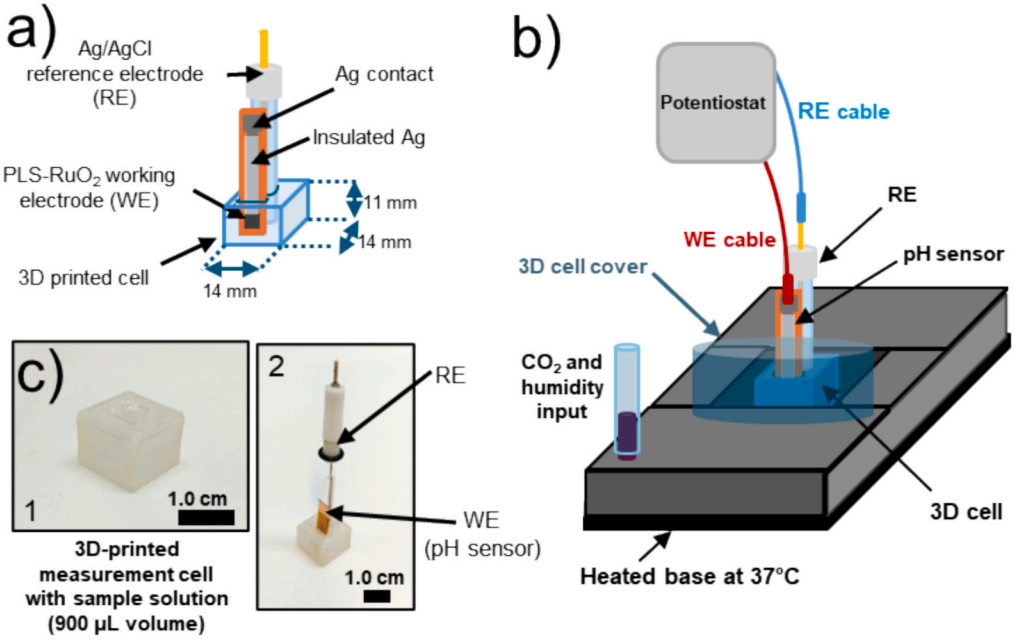

Scheme 1. (a) Schematic representation (with dimensions) of the 3D printed cell employed for cell culture pH measurements. Pictures of the 3D printed measurement cell with (2) and without (1) the electrodes. (b) Schematic representation of the experimental setup (microincubator and 3D cell) used for cell culture pH measurements.

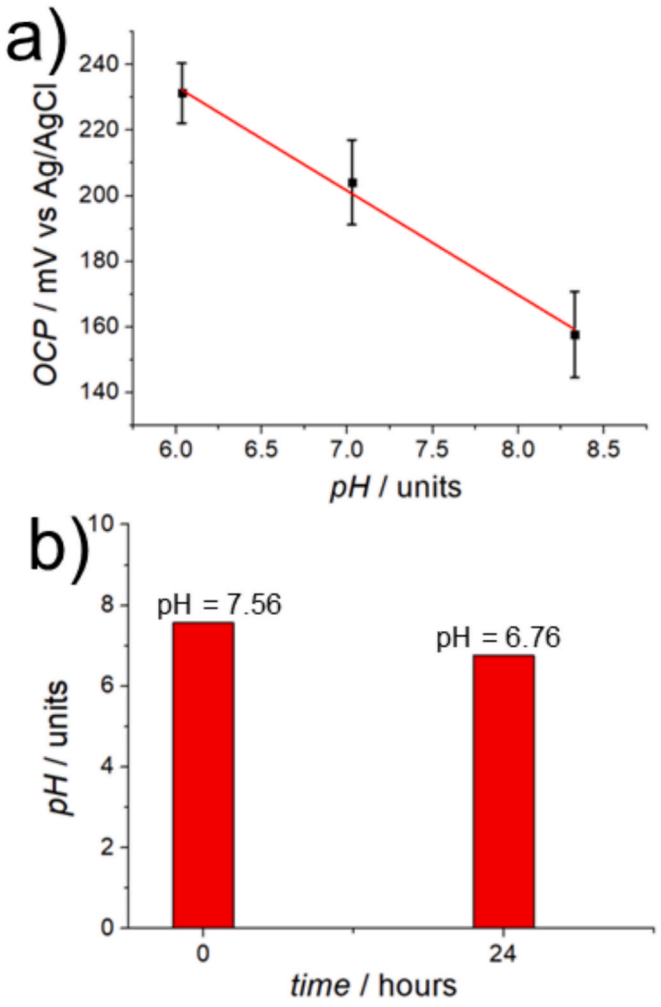

Fig. 6. (a) Average calibration graph recorded by using three PLS-RuO_2 electrodes (average Ru loading = 210.6 $\mu g_{Ru}/cm^2$) in cell culture medium. Slope = −31.8 mV/unit; $R^2 = 0.990$. (b) pH variation of the cell culture growth medium over 24 hours, measured by using a PLS-RuO_2 pH sensor.

losses. PLS-RuO_2 patterns did not require any further thermal treatment and were used to construct fully inkjet-printed PLS-RuO_2 thin film electrodes and PLS-RuO_2-modified graphene electrodes as working electrodes for potentiometric and amperometric sensing. Importantly, the demonstrated method produces RuO_2 electrodes based on very low material consumption rates, which is essential for future applications when this material can't be replaced with renewable compounds.

PLS-RuO_2 film electrodes in voltammeric methods showed the characteristic electrochemical behaviour, *i.e.*, capacitive currents and redox peaks, of the RuO_2 system. PLS-RuO_2-modified graphene electrodes were applied for L-Cysteine detection showing an electrocatalytic effect (−362 mV) and superior sensing performances in the presence of interferent species (*i.e.*, uric acid) in respect to bare graphene. PLS has confirmed in many ways its high potential. When using more intense light sources, PLS can open the way to produce many new materials, such as by inserting metal single atoms into graphene, to fabricate more efficient electrocatalysts, which can be employed in energy conversion applications [55]. The key role of inkjet printing is the controlled loading of the metal precursor on the surface generating a very small reaction volume for highly efficient surface confined light induced material synthesis.

The PLS-RuO_2 thin film electrodes showed a Nernstian response in a pH range from 2 to 12 and their application as pH sensor in real samples was demonstrated. The PLS-RuO_2 film electrodes were used to detect the acidification of a cancer cell culture.

CRediT authorship contribution statement

Stefano Gianvittorio: Writing – original draft, Methodology, Investigation, Data curation, Conceptualization. **Marco Malferrari:** Methodology, Investigation. **Horst Pick:** Resources, Investigation. **Stefania Rapino:** Supervision, Resources, Conceptualization. **Andreas Lesch:** Writing – review & editing, Supervision, Resources, Methodology, Conceptualization.

Declaration of competing interest

The authors declare that they have no known competing financial interests or personal relationships that could have appeared to influence the work reported in this paper.

Acknowledgements

Dr. Mounir Mensi (EPFL, ISIC-XRDSAP) is thanked for having performed the XPS measurements. Dr. Francesca Ospitali (University of Bologna) is thanked for the support in the SEM-EDS analysis. Prof. Giovanni Valenti (University of Bologna) is thanked for proving the portable pH electrode.

Appendix A. Supplementary material

Supplementary data to this article can be found online at https://doi.org/10.1016/j.bioelechem.2025.108909.

Data availability

Data will be made available on request.

References

[1] K. Singh, B.S. Lou, J.L. Her, S.T. Pang, T.M. Pan, Super Nernstian pH response and enzyme-free detection of glucose using sol-gel derived RuOx on PET flexible-based extended-gate field-effect transistor, Sens. Actuators B 298 (2019), https://doi.org/10.1016/j.snb.2019.126837.

[2] J. Wang, Q.H. Zhang, Q.Y. Huang, Y.H. Xiao, X.R. Li, X.H. Gu, F.H. Cao, In-situ pH monitoring of pre-notched X80 pipeline steel using an all-solid-state Pt/RuOx ultra-micro pH sensor, Sens. Actuators B 407 (2024), https://doi.org/10.1016/j.snb.2024.135484.

[3] K. Prabhu, S.J. Malode, N.P. Shetti, S. Pandiaraj, A. Alodhayb, M. Muthuramamoorthy, Determination of fungicide at Ru-doped TiO2/reduced graphene oxide decorated electrochemical sensor, Microchem. J. 197 (2024), https://doi.org/10.1016/j.microc.2023.109722.

[4] V. Vijayabala, N. Senthilkumar, K. Nehru, R. Karvembu, Hydrothermal synthesis and characterization of ruthenium oxide nanosheets using polymer additive for supercapacitor applications, J. Mater. Sci. Mater. Electron. 29 (2018) 323–330, https://doi.org/10.1007/s10854-017-7919-x.

[5] S. Jeon, J.H. Jeong, H. Yoo, H.K. Yu, B.H. Kim, M.H. Kim, RuO2 nanorods on electrospun carbon nanofibers for supercapacitors, ACS Appl. Nano Mater. 3 (2020) 3847–3858, https://doi.org/10.1021/acsanm.0c00579.

[6] M.Y. Chung, C.T. Lo, High-performance binder-free RuO2/electrospun carbon fiber for supercapacitor electrodes, Electrochim. Acta 364 (2020), https://doi.org/10.1016/j.electacta.2020.137324.

[7] W. Lonsdale, S.P. Shylendra, S. Brouwer, M. Wajrak, K. Alameh, Application of ruthenium oxide pH sensitive electrode to samples with high redox interference, Sens. Actuators B 273 (2018) 1222–1225, https://doi.org/10.1016/j.snb.2018.07.022.

[8] A. Sardarinejad, D.K. Maurya, K. Alameh, The effects of sensing electrode thickness on ruthenium oxide thin-film pH sensor, Sens. Actuators, A 214 (2014) 15–19, https://doi.org/10.1016/j.sna.2014.04.007.

[9] V. Saucedo, B. Wolk, A. Arroyo, C.D. Feng, Studying the drift of in line pH measurements in cell culture, Biotechnol. Prog. 27 (2011) 885–890, https://doi.org/10.1002/btpr.598.

[10] P. Veerakumar, S.T. Hung, P.Q. Hung, K.C. Lin, Review of the design of ruthenium-based nanomaterials and their sensing applications in electrochemistry, J. Agric. Food Chem. 70 (2022) 8523–8550, https://doi.org/10.1021/acs.jafc.2c01856.

[11] C. Anjalidevi, V. Dharuman, J. Shankara Narayanan, Non enzymatic hydrogen peroxide detection at ruthenium oxide-gold nano particle-Nafion modified electrode, Sens. Actuators B 182 (2013) 256–263, https://doi.org/10.1016/j.snb.2013.03.006.

[12] A.S. Kumar, P.Y. Chen, S.H. Chien, J.M. Zen, Development of an enzymeless/mediatorless glucose sensor using ruthenium oxide-Prussian blue combinative analogue, Electroanalysis 17 (2005) 210–222, https://doi.org/10.1002/elan.200403086.
[13] N.P. Shetti, D.S. Nayak, S.J. Malode, R.R. Kakarla, S.S. Shukla, T.M. Aminabhavi, Sensors based on ruthenium-doped TiO 2 nanoparticles loaded into multi-walled carbon nanotubes for the detection of flufenamic acid and mefenamic acid, Anal. Chim. Acta 1051 (2019) 58–72, https://doi.org/10.1016/j.aca.2018.11.041.
[14] Y.G. Lee, B.X. Liao, Y.C. Weng, Ruthenium oxide modified nickel electrode for ascorbic acid detection, Chemosphere 173 (2017) 512–519, https://doi.org/10.1016/j.chemosphere.2017.01.086.
[15] H. Kivrak, K. Selçuk, O.F. Er, N. Aktas, Electrochemical cysteine sensor on novel ruthenium based ternary catalyst, Int. J. Electrochem. Sci. 16 (2021) 1–17, https://doi.org/10.20964/2021.05.48.
[16] Y. Murakami, J. Li, D. Hirose, S. Kohara, T. Shimoda, Solution processing of highly conductive ruthenium and ruthenium oxide thin films from ruthenium-amine complexes, J. Mater. Chem. C 3 (2015) 4490–4499, https://doi.org/10.1039/c5tc00675a.
[17] N.C. Raut, K. Al-Shamery, Inkjet printing metals on flexible materials for plastic and paper electronics, J. Mater. Chem. C 6 (2018) 1618–1641, https://doi.org/10.1039/c7tc04804a.
[18] M. Layani, M. Grouchko, S. Shemesh, S. Magdassi, Conductive patterns on plastic substrates by sequential inkjet printing of silver nanoparticles and electrolyte sintering solutions, J. Mater. Chem. 22 (2012) 14349–14352, https://doi.org/10.1039/c2jm32789a.
[19] H.S. Kim, S.R. Dhage, D.E. Shim, H.T. Hahn, Intense pulsed light sintering of copper nanoink for printed electronics, Appl. Phys. A Mater. Sci. Process. 97 (2009) 791–798, https://doi.org/10.1007/s00339-009-5360-6.
[20] I. Reinhold, C.E. Hendriks, R. Eckardt, J.M. Kranenburg, J. Perelaer, R. R. Baumann, U.S. Schubert, Argon plasma sintering of inkjet printed silver tracks on polymer substrates, J. Mater. Chem. 19 (2009) 3384–3388, https://doi.org/10.1039/b823329b.
[21] H.M. Lee, H.B. Lee, D.S. Jung, J.Y. Yun, S.H. Ko, S.B. Park, Solution processed aluminum paper for flexible electronics, Langmuir 28 (2012) 13127–13135, https://doi.org/10.1021/la302479x.
[22] B. Lee, Y. Kim, S. Yang, I. Jeong, J. Moon, A low-cure-temperature copper nano ink for highly conductive printed electrodes, Curr. Appl Phys. 9 (2009) e157–e160, https://doi.org/10.1016/j.cap.2009.03.008.
[23] P.J. Smith, A. Morrin, Reactive inkjet printing, J. Mater. Chem. 22 (2012) 10965–10970, https://doi.org/10.1039/c2jm30649b.
[24] M. Abulikemu, E.H. Da'As, H. Haverinen, D. Cha, M.A. Malik, G.E. Jabbour, Insitu synthesis of self-assembled gold nanoparticles on glass or silicon substrates through reactive inkjet printing, Angew. Chem. - Int. Ed. 53 (2014) 420–423, https://doi.org/10.1002/anie.201308429.
[25] R. Zou, Y. Wang, M. Hu, Y. Wei, T. Fujita, Analysis of ruthenium electrodeposition in the nitric acid medium, J. Phys. Chem. C 126 (2022) 4329–4337, https://doi.org/10.1021/acs.jpcc.1c09371.
[26] A. Lesch, Print-light-synthesis of platinum nanostructured indium-tin-oxide electrodes for energy research, Adv. Mater. Technol. 3 (2018), https://doi.org/10.1002/admt.201700201.
[27] V. Costa Bassetto, M. Mensi, E. Oveisi, H.H. Girault, A. Lesch, Print-light-synthesis of Ni and NiFe-nanoscale catalysts for oxygen evolution, ACS Appl. Energy Mater. 2 (2019) 6322–6331, https://doi.org/10.1021/acsaem.9b00957.
[28] W.O. Silva, V. Costa Bassetto, D. Baster, M. Mensi, E. Oveisi, H.H. Girault, Oxidative print light synthesis thin film deposition of Prussian blue, ACS Appl. Electron. Mater. 2 (2020) 927–935, https://doi.org/10.1021/acsaelm.9b00854.
[29] E. Maiorano, S. Gianvittorio, M. Lanzi, D. Tonelli, H. Pick, A. Lesch, Print-light-synthesis of gold thin film electrodes for electrochemical sensing, Adv. Mater. Technol. 8 (2023), https://doi.org/10.1002/admt.202202039.
[30] K.M. Daly, S. Jimenez-Villegas, B. Godwin, M.A.W. Schoen, O. Calderon, N. Chen, S. Trudel, A comparison of photodeposited RuOx for alkaline water electrolysis, ACS Appl. Energy Mater. 6 (2023) 1449–1458, https://doi.org/10.1021/acsaem.2c03339.
[31] Y. Murakami, J. Li, T. Shimoda, Highly conductive ruthenium oxide thin films by a low-temperature solution process and green laser annealing, Mater. Lett. 152 (2015) 121–124, https://doi.org/10.1016/j.matlet.2015.03.084.
[32] G. Šekularac, M. Košević, I. Drvenica, A. Dekanski, V. Panić, B. Nikolić, Titanium coated with high-performance nanocrystalline ruthenium oxide synthesized by the microwave-assisted sol–gel procedure, J. Solid State Electrochem. 20 (2016) 3115–3123, https://doi.org/10.1007/s10008-016-3343-z.
[33] J. Chen, M. Saeidi-Javash, M. Palei, M. Zeng, Y. Du, K. Mondal, M.D. McMurtrey, A.J. Hoffman, Y. Zhang, Printing noble metal alloy films with compositional gradient, Appl. Mater. Today 27 (2022), https://doi.org/10.1016/j.apmt.2022.101405.
[34] M. Taheri, M. Ketabi, A.M. Al Shboul, S. Mahinnezhad, R. Izquierdo, M.J. Deen, Integrated pH sensors based on RuO2/GO nanocomposites fabricated using the aerosol jet printing method, ACS Omega 8 (2023) 46794–46803, https://doi.org/10.1021/acsomega.3c06309.
[35] S.D. Hoath, Fundamentals of Inkjet Printing - The Science of Inkjet and Droplets, Wiley VCH, 2016.
[36] S. Gianvittorio, D. Tonelli, A. Lesch, Print-light-synthesis for single-step metal nanoparticle synthesis and patterned electrode production, Nanomaterials 13 (2023), https://doi.org/10.3390/nano13131915.
[37] X. Que, T. Lin, S. Li, X. Chen, C. Hu, Y. Wang, M. Shi, J. Peng, J. Li, J. Ma, M. Zhai, Radiation synthesis of size-controllable ruthenium-based electrocatalysts for hydrogen evolution reaction, Appl. Surf. Sci. 541 (2021), https://doi.org/10.1016/j.apsusc.2020.148345.
[38] Q. Zhang, M. Zhai, J. Peng, Y. Hao, J. Li, Radiation-induced synthesis and characterization of ruthenium/carboxymethylated-chitosan nanocomposites, Nucl. Instrum. Methods Phys. Res., Sect. B (2012) 334–340.
[39] F. Li, Y. Shang, Z. Ding, H. Weng, J. Xiao, M. Lin, Efficient extraction and separation of palladium (Pd) and ruthenium (Ru) from simulated HLLW by photoreduction, Sep. Purif. Technol. 182 (2017) 9–18, https://doi.org/10.1016/j.seppur.2017.03.029.
[40] J. Belloni, M. Mostafavi, H. Remita, J.L. Marignier, M.O. Delcourt, Radiation-induced synthesis of mono- and multi-metallic clusters and nanocolloids, New J. Chem. 22 (1998) 1239–1255, https://doi.org/10.1039/a801445k.
[41] Y. Zhao, Y. Luo, X. Yang, Y. Yang, Q. Song, Tunable preparation of ruthenium nanoparticles with superior size-dependent catalytic hydrogenation properties, J. Hazard. Mater. 332 (2017) 124–131, https://doi.org/10.1016/j.jhazmat.2017.03.004.
[42] A.E. Newkirk, D.W. McKee, Thermal decomposition of rhodium, iridium, and ruthenium chlorides, J. Catal. 11 (1968) 370–377, https://doi.org/10.1016/0021-9517(68)90061-4.
[43] W.K. Jóźwiak, T.P. Maniecki, Influence of atmosphere kind on temperature programmed decomposition of noble metal chlorides, Thermochim Acta 435 (2005) 151–161, https://doi.org/10.1016/j.tca.2005.05.006.
[44] D.J. Morgan, Resolving ruthenium: XPS studies of common ruthenium materials, Surf. Interface Anal. 47 (2015) 1072–1079, https://doi.org/10.1002/sia.5852.
[45] P. Froment, M.J. Genet, M. Devillers, Surface reduction of ruthenium compounds with long exposure to an X-ray beam in photoelectron spectroscopy, J. Electron Spectrosc. Relat. Phenom. 104 (1999) 119–126, https://doi.org/10.1016/s0368-2048(98)00462-9.
[46] R. Kötz, S. Stucki, D. Scherson, D.M. Kolb, In-situ identification of RuO4 as the corrosion product during oxygen evolution on ruthenium in acid media, J. Electroanal. Chem. 172 (1984) 211–219, https://doi.org/10.1016/0022-0728(84)80187-4.
[47] J. Llopis, M. Vázquez, Passivation of ruthenium in hydrochloric acid solution, Electrochim. Acta 11 (1966) 633–640, https://doi.org/10.1016/0013-4686(66)87007-X.
[48] P. Shakkthivel, S.M. Chen, Simultaneous determination of ascorbic acid and dopamine in the presence of uric acid on ruthenium oxide modified electrode, Biosens. Bioelectron. 22 (2007) 1680–1687, https://doi.org/10.1016/j.bios.2006.07.026.
[49] T. Rehman, M.A. Shabbir, M. Inam-Ur-Raheem, M.F. Manzoor, N. Ahmad, Z. W. Liu, M.H. Ahmad, A. Siddeeg, M. Abid, R.M. Aadil, Cysteine and homocysteine as biomarker of various diseases, Food Sci. Nutr. 8 (2020) 4696–4707, https://doi.org/10.1002/fsn3.1818.
[50] H.R. Zare, F. Chatraei, Preparation and electrochemical characteristics of electrodeposited acetaminophen on ruthenium oxide nanoparticles and its role as a sensor for simultaneous determination of ascorbic acid, dopamine and N-acetyl-l-cysteine, Sens. Actuators B 160 (2011) 1450–1457, https://doi.org/10.1016/j.snb.2011.10.012.
[51] M. Dório, I.M. Benseñor, P. Lotufo, I.S. Santos, R. Fuller, Reference range of serum uric acid and prevalence of hyperuricemia: a cross-sectional study from baseline data of ELSA-Brasil cohort, Adv. Rheumatol. 62 (2022), https://doi.org/10.1186/s42358-022-00246-3.
[52] S. Gläb, A. Hulanicki, G. Edwall, F. Folke, I. Ingman, W.F. Koch, Metal-metal oxide and metal oxide electrodes as pH sensors, Crit. Rev. Anal. Chem. 21 (1989) 29–47, https://doi.org/10.1080/10408348908048815.
[53] H. Chen, Y. Li, H. Li, X. Chen, H. Fu, D. Mao, W. Chen, L. Lan, C. Wang, K. Hu, J. Li, C. Zhu, I. Evans, E. Cheung, D. Lu, Y. He, A. Behrens, D. Yin, C. Zhang, NBS1 lactylation is required for efficient DNA repair and chemotherapy resistance, Nature 631 (2024) 663–669, https://doi.org/10.1038/s41586-024-07620-9.
[54] A. Soldà, G. Valenti, M. Marcaccio, M. Giorgio, P.G. Pelicci, F. Paolucci, S. Rapino, Glucose and lactate miniaturized biosensors for SECM-based high-spatial resolution analysis: a comparative study, ACS Sensors 2 (2017) 1310–1318, https://doi.org/10.1021/acssensors.7b00324.
[55] H. Gong, Z. Gong, J. Liu, G. Ye, H. Fei, General and ultrafast photothermal synthesis of atomic metal-nitrogen-carbon catalysts for H2O2 electrosynthesis, Adv. Funct. Mater. 34 (2024), https://doi.org/10.1002/adfm.202316438.